J. Bangladesh Acad. Sci. 49(2); 271-285: December 2025 DOI:https://doi.org/10.3329/jbas.v49i2.82006

Journal of Bangladesh Academy of Sciences

Journal homepage: http://www.bas.org.bd/publications/jbas.html

Research Article

AC impedance analysis of $Bi_{1-x}Y_xFe_{0.7}Mn_{0.3}O_3$ multiferroic ceramics

Sonet Kumar Saha[1*], Md. Ashraf Ali[2,] and AKM Akther Hossain

Department of Physics, Bangladesh University of Engineering and Technology, Dhaka, Bangladesh

ARTICLE INFO

Article History

Received: 01 June 2025

Revised: 29 September 2025

Accepted: 12 October 2025

Keywords: $Bi_{1-x}Y_xFe_{0.7}Mn_{0.3}O_3$; EDX, Xray diffraction; Dielectric properties; Impedance analysis; AC conductivity.

ABSTRACT

In this paper, the AC impedance properties of $Bi_{1-x}Y_xFe_{0.7}Mn_{0.3}O_3$ (BYFMO) ceramics with x values from 0.00 to 0.20 were studied. It was manufactured via solid-state chemistry, and during manufacturing, sintering at temperatures was at 800, 825, and 850°C, and optimal bulk density was at 825°C. X-ray diffraction investigation verified differences in lattice parameters resulting from doping-induced strain and defect structures, suggesting the presence of a rhombohedral phase along with small secondary phases. Field Emission Scanning Electron Microscopy (FESEM) demonstrated a porous microstructure with grain sizes ranging from 1.22 to 1.89 µm. Energy Dispersive X-ray spectroscopy confirmed the elemental composition. The dielectric constant (ε′) demonstrated a frequency-dependent reduction, stabilizing beyond 10 kHz. At 100Hz, ε′ rose from 65 to 78 at 100 Hz with increasing Y doping due to a reduction in the quantities of oxygen vacancies. Impedance spectroscopy revealed distinct semicircular patterns in undoped material, indicating grain and grain boundary effects, while doped samples mostly demonstrated grain conduction, elucidating multiferroic electrical transport mechanisms. We have gotten the maximum grain resistance 199.02 MΩ for highest doping at x = 0.20.

Introduction

Multiferroic materials are a special kind of material because they simultaneously exhibit at least two ferroic properties. One is ferromagnetism (ordered magnetic moments), and another is ferroelectricity (spontaneous electric polarization), or ferroelasticity (spontaneous strain). And the magneto-electric coupling between the ferroic orders is present in these materials. This coupling can be controlled by an external electric or magnetic field. As a result, they have potential in multifunctional applications, including spintronics, data storage, sensors, energy harvesting, and optoelectronics (Yin and Mi, 2020; Verma, 2020; Muneeswaran et al., 2021; Wang et al., 2020). Bismuth ferrite ($BiFeO_3$, BFO) is a notable single phase multiferroic substance. It is characterized by a rhombohedrally deformed perovskite structure (space group R3c). It demonstrates a significant ferroelectric transition temperature (T_e = 827 °C) and an antiferromagnetic Néel temperature (T_n = 377 °C) (Scott, 2007; Ramesh and Spaldin, 2007; Zatsiupa et al., 2014). These features, along with the simultaneous presence of electric and magnetic ordering at room temperature, make BFO a compelling choice for sensitive device applications. Although it has advantageous properties but BFO faces the major challenges. These are leakage currents at higher levels and inconsistencies in polarization values

[*]Corresponding author:< sonnet4321@gmail.com, ashrafphy31@cuet.ac.bd>

[1]*Department of Electrical and Electronic Engineering, Z. H. Sikder University of Science and Technology, Shariatpur, Bangladesh*

[2]*Department of Physics, Chittagong University of Engineering and Technology, Chattogram, Bangladesh*

between bulk ceramics and thin films (Teague et al., 1970; Wang et al., 2004). For example, thin films have a polarization of 90–100 μC/cm^{2}, which subjects them to heteroepitaxial constraints; on the other hand, bulk materials exhibit values roughly one-tenth as high. Additionally, structural defects, oxygen vacancies, and non-stoichiometry are present in the material, which impede its practical application (Palkar et al., 2002). To overcome these restrictions, prominent researchers have investigated replacing atoms at both the A- and B-sites of the perovskite lattice. For examples, the substitution of trivalent ions, including La^{3+} (Zhang et al., 2006), Eu^{3+} (Huong et al., 2017), and Gd^{3+} (Singh et al., 2018), as well as divalent ions such as Ca^{2+} (Chen et al., 2010), Sr^{2+} (Varshney and Kumar, 2013), and Ba^{2+} (Chauhan et al., 2013) at the A-site for reducing oxygen vacancies and altering the ferroelectric and magnetic characteristics of a material and also B-site substitutions with ions such as Nb^{5+} (Singh and Yadav, 2012), Ti^{4+} (Minh et al., 2024), and Cr^{3+} (Agrawal et al., 2025) for improving the material's structural, magnetic, and electrical properties. And there are also Co-substitution, such as (Mn, Nb) (Chung et al., 2006), (La, Co) (Gu et al., 2016), (La, V) (Yu et al., 2008), (Pr, Ti) (Wu et al., 2016), and (Na, Ti) (Das Adhikary et al., 2023), at both A- and B-sites for modifying the features of BFO. So, it can be said that the choice of elements for co-substitution at the A- and B-sites in $BiFeO_3$ depends on their influence on the characteristics of the material. Recent studies by Wu et al. (2012) show that the A-site of Bismuth Ferrite (BFO) substituted with Yttrium (Y^{3+}) causes inner lattice stress because its ionic radius is less than that of Bi^{3+}. Consequently, a structural change from rhombohedral (R3c) to orthorhombic (Pnma) symmetry occurred at approximately x = 0.10. This phase transition is related to a ferroelectric-to-paraelectric transformation and significant alterations in magnetization behavior (Wu et al., 2012). Another investigation by Gautam et al. (2012) demonstrates Y-doped $BiFeO_3$ samples exhibit superior dielectric characteristics and increased saturation magnetization, and by Luo et al. (2012) observed a reduction in leakage current with higher Y^{3+} concentration. Another study by Chen et al. (2015) and Chen (2014) illustrated that Mn substitution at the B-site has several effects on BFO. The effects include modifications in ferroelectric and magnetic characteristics, reduced leakage current, and increased dielectric constant. But few studies have examined the dielectric properties, AC conductivity, and impedance characteristics of BFO under the joint effects of Y and Mn co-substitution. This study synthesized $Bi_{1-x}Y_xFe_{0.7}Mn_{0.3}O_3$ ceramics (x=0.00–0.20) using the solid-state reaction technique and investigated the impact of Y^{3+} doping on the dielectric properties, AC conductivity, and impedance characteristics of the material. This study also explores the potential application of Y–Mn co-substituted BFO. It is noted that multiferroic materials need high dielectric properties to enhance their significance for upcoming electronic devices such as memory, sensors, and tunable microwave devices.

Experimental Details

Synthesis of $Bi_{1-x}Y_xFe_{0.7}Mn_{0.3}O_3$ Ceramics

Using high-purity precursors obtained from Sigma-Aldrich (each 99.99% pure) – specifically bismuth (III) oxide (Bi_2O_3), iron(III) oxide (Fe_2O_3), yttrium(III) oxide (Y_2O_3), and manganese carbonate ($MnCO_3$) – $Bi_{1-x}Y_xFe_{0.7}Mn_{0.3}O_3$ ceramic samples (where x=0.00, 0.05, 0.10, 0.15, 0.20) were prepared via a standard solid-state reaction method. The components were accurately weighed to obtain the required stoichiometric ratios using an electronic balance (Shimadzu, AX 120). The initial powders were meticulously combined with acetone in an agate mortar and pestle for 3 hours to achieve a uniform dispersion. Then, the blended powder was calcined at 700°C for 6 hours in an ambient atmosphere using a programmable furnace (Nabertherm P330) to facilitating phase formation. After calcination, the resultant powders were meticulously crushed and reground for 1 hour, then compressed into cylindrical pellets with a diameter of 12 mm using a uniaxial hydraulic press at 200 MPa. Then, the compacted pellets were sintered at 800°C, 825°C, and 850°C for 12 hours. The heating rate was sustained at 10°C/min, succeeded by a regulated cooling rate of 5°C/min in ambient air. The sintered pellets were carefully polished to prepare the samples for future characterization. This entailed employing silicon carbide abrasive sheets with ever finer grit sizes until a uniformly smooth and even surface was attained across all samples.

Characterizations

Crystal and Microstructural Characterization

The crystal structure was analyzed using an X-ray diffractometer (Philips PANalytical X'PERT-PRO). Where Cu-Kα radiation is an X-ray source with λ=1.5406 Å. The operation setup was set to 40 kV and 30 mA. The X-ray scan for data collection was performeed over a 2θ range of 20° to 60° at a rate of 1°/min. Here, the instrument was calibrated time-to-time using a standard silicon sample. It ensures the accuracy and reliability of the measurements.

A FESEM with model JEOL JSM 7600F was employed to examine the microstructural properties of the samples. And, EDX spectroscopy was conducted to determine the elemental composition and also verify the chemical consistency of the materials.

Density and Dielectric Properties

The following formula was used to measure the bulk density (ρ_B) of all samples:

$$\rho_B = \frac{m}{\pi r^2 t}$$

where m = mass, r = radius, and t = the thickness of the pellet. To assess the dielectric property, two metallic conductors were connected to the opposing faces of the prepared samples by using silver paste as electrodes. The samples were then heated in an oven for 1 hour. Consequently, it ensures the complete curing of the silver paste and establishes a robust electrical contact without affecting the properties of the materials. The dielectric constant ε' was calculated using the equation:

$$\varepsilon' = \frac{Ct}{\varepsilon_o A}$$

where C, t, ε_o and A are the capacitance, the sample thickness, the permittivity of free space, and electrode area, respectively. AC conductivity σ_{ac} was determined using the relation: $\sigma_{ac} = \omega\varepsilon'\varepsilon_o \tan\delta_{AC}$ where ω, tanδ, ε′ are angular frequency, dielectric loss, and the dielectric constant, respectively. All dielectric properties were measured using a Wayne Kerr Impedance Analyzer (Model 6500B) over a frequency range of 100 Hz to 120 MHz.

Result and Discussion

Structural Analysis with XRD

Fig. 1 presents the X-ray diffraction (XRD) patterns. The patterns are drawn from X-ray diffraction data collected on a series of $Bi_{1-x}Y_xFe_{0.7}Mn_{0.3}O_3$ samples using an X-ray diffractometer. From these patterns, the crystalline structures for Y-doping concentrations at x=0.00, 0.05, 0.10, 0.15, and 0.20 can be evaluated. Systematic variations in the XRD profiles are observed across different x values, revealing the structural evolution and phase purity of these materials. Here, the observed diffraction peaks exhibit a pattern similar to that of $BiFeO_3$ (JCPDS Card No. 71-2494). Although secondary phase peaks corresponding to Bi- or Fe-rich phases, specifically $Bi_2Fe_4O_9$ and $Bi_{25}FeO_{40}$, were detected across all samples. Those are denoted by asterisk (*) in Fig. 1. That kind of finding is consistent with previous studies by Dao et al. (2013) and Xu et al. (2009). Despite these secondary phases, all primary diffraction peaks for various x align with the rhombohedral R3c crystal structure, characteristic of $BiFeO_3$.

(a)

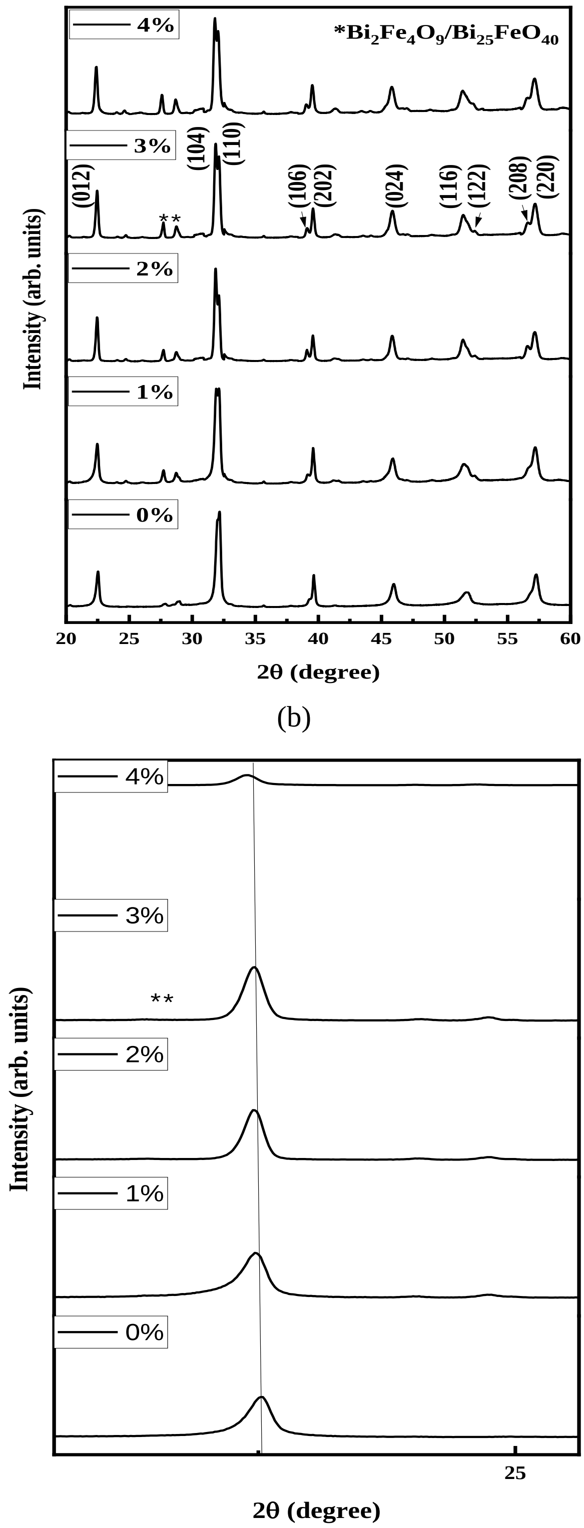

Fig. 1 (a) XRD patterns of $Bi_{1-x}Y_xFe_{0.7}Mn_{0.3}O_3$ (x=0.00, 0.05, 0.10, 0.15, and 0.20) compositions sintered at 825 °C (b) enlarged view.

Notably, increasing Y doping concentration in our samples shifted the diffraction peaks to lower Bragg angles Fig. 1(b)) indicating the successful incorporation of Y ions into the parent lattice and their influence on its structure. This structure was further confirmed by performing a Rietveld refinement analysis using the FullProf software package, which provided impurity phases for composition as shown in Fig. 1(c).

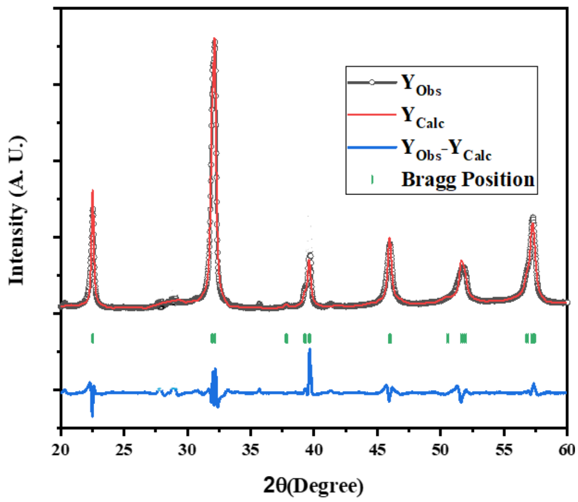

Fig. 1 (c) XRD refinement patterns of $Bi_{1-x}Y_xFe_{0.7}Mn_{0.3}O_3$ (x=0.00) compositions sintered at 825 °C.

The tolerance factor (t) is a useful tool for determining the stability of perovskite compounds. This factor is calculated as follows: $t = (r_A + r_O)/\sqrt{2}(r_B+r_O)$, where r_A is the average ionic radius of Bi^{3+} and Y^{3+} ions, r_O for O^{2-} ion, and r_B for Fe^{3+}, Fe^{4+}, and Mn^{3+} ions. In this investigation, a decreasing trend in the tolerance factor was observed with increasing Yttrium (Y) doping concentration, specifically from t = 0.84023 for the undoped (x= 0.0) composition to t = 0.83124 for the x = 0.20 doped sample. This reduction inherently expresses that a mismatch between the ionic radii of the constituent cations and the oxygen anions has increased. So, it enhances the thermodynamic driving force for cooperative octahedral tilting or rotation. Consequently, a structural distortion occurs in doped samples (Karimi et al., 2009).

Density of the compositions

Fig. 2 illustrates the influence of sintering temperature on the bulk density for various Y-doping samples. At first, there is a clear correlation between bulk density and sintering temperatures; it increases with rising temperature and reaches a maximum at 825°C.

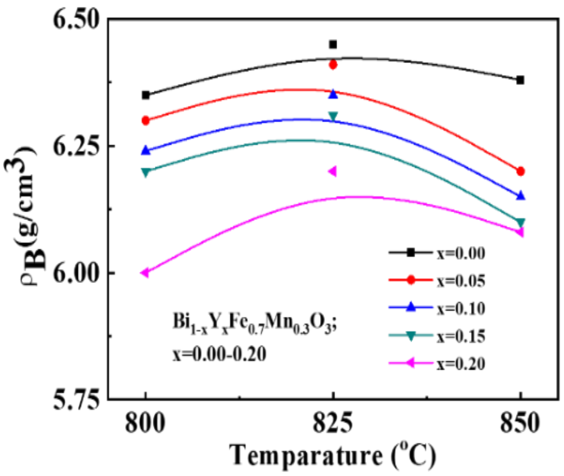

Fig. 2 Dependence of bulk density, ρ_B on sintering temperature for various $Bi_{1-x}Y_xFe_{0.7}Mn_{0.3}O_3$.

Nevertheless, additional increases in temperature result in a reduction of bulk density. This pattern can be ascribed to the interaction and the correlation between grain expansion and the loss of Bi_2O_3. Initially, thermal energy during sintering facilitates grain growth. As a result, grain boundaries expand into pores, reducing pore volume and enhancing material densification. On the other hand, an opposite behavior is observed above 825°C. It may occur because Bi_2O_3 evaporation becomes significant, counteracting the densification effect. Moreover, its melting point at approximately 825°C contributes to the observed density reduction. Based on these findings, an optimal sintering temperature for our samples is 825°C. It recommends that subsequent characterization studies of the samples be carried out at this temperature.

Microstructure of $Bi_{1-x}Y_xFe_{0.7}Mn_{0.3}O_3$ (BYFMO)

Fig. 3 presents FESEM micrographs of the studied samples. From micrographs, randomly oriented microstructure and non-uniform grains with intergranular porosity are observed. The factors influencing this grain growth depend on the interplay between the thermodynamic driving forces promoting grain boundary migration and the kinetic hindering imposed by pervasive porosity. When driving forces are inhomogeneous, non-uniform grain growth occurs, whereas when forces are homogeneous, uniform grain sizes are available (Miah et al., 2016). The average grain size (D) was quantified from FESEM micrographs using ImageJ. The corresponding grain size distribution histograms, fitted to a Gaussian distribution, are shown in the right panel of each image. The calculated D values range from 1.22 to 1.89 µm. This anomalous value suggests that the sintering temperature may not have been optimal for this composition. But, to study the effect of variation in Y contents, the sintering temperature was kept fixed for all compositions. A correlation with D and elevated Y content. This relation can arise from the role of fine particles as high-diffusion pathways, which promote grain expansion (Basiri et al., 2014).

EDX Analysis

EDX spectroscopy is an effective technique for determining the elemental composition of the samples. Analysis of various points across the samples (Fig. 4) revealed the experimental and calculated mass percentages of elements. EDX spectra ensured that all raw compositions are present in the sample. The details of elemental compositions are tabulated in the accompanying EDX spectra.

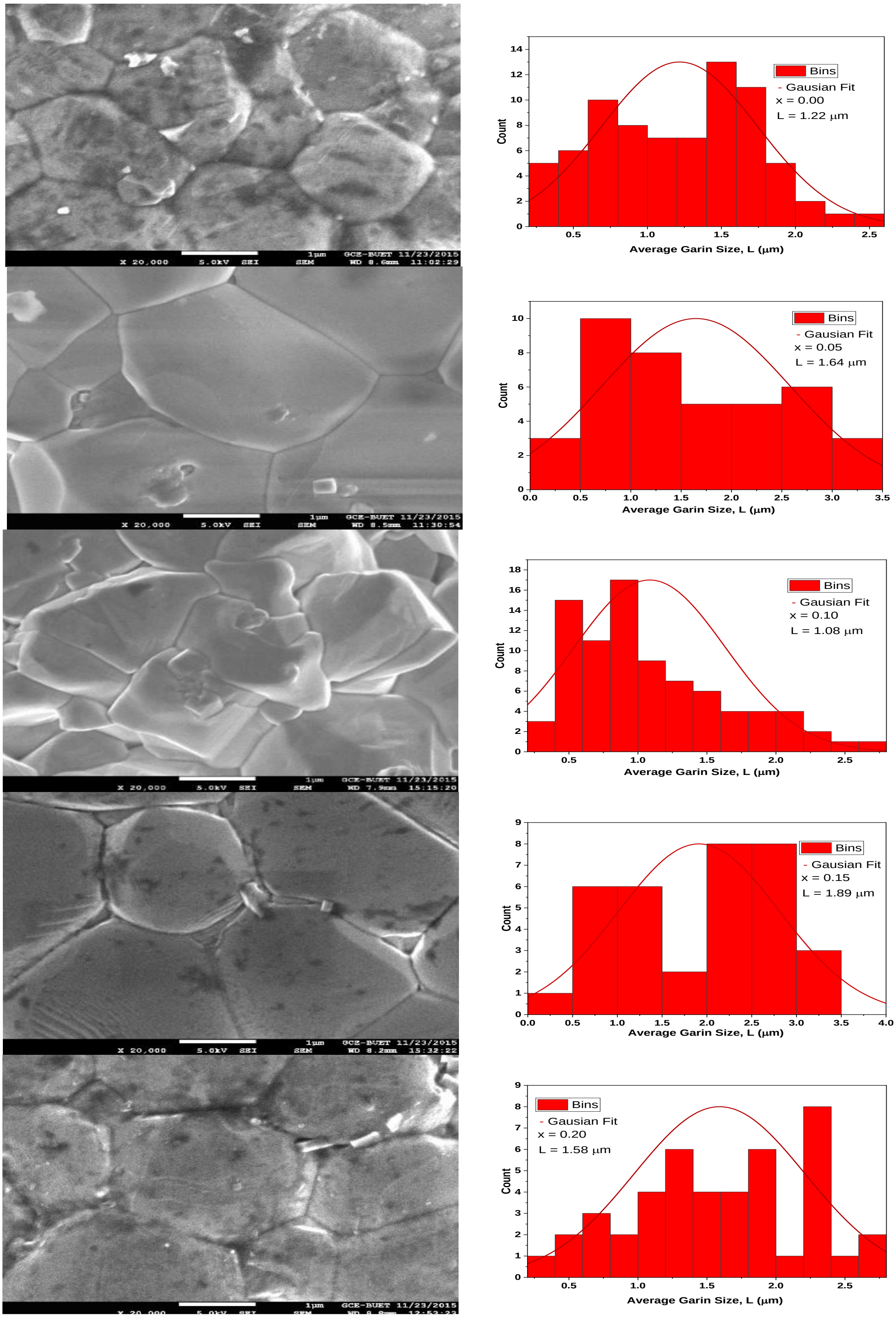

Fig. 3 FESEM micrographs of various $Bi_{1-x}Y_xFe_{0.7}Mn_{0.7}O_3$ ceramics sintered at 825 °C.

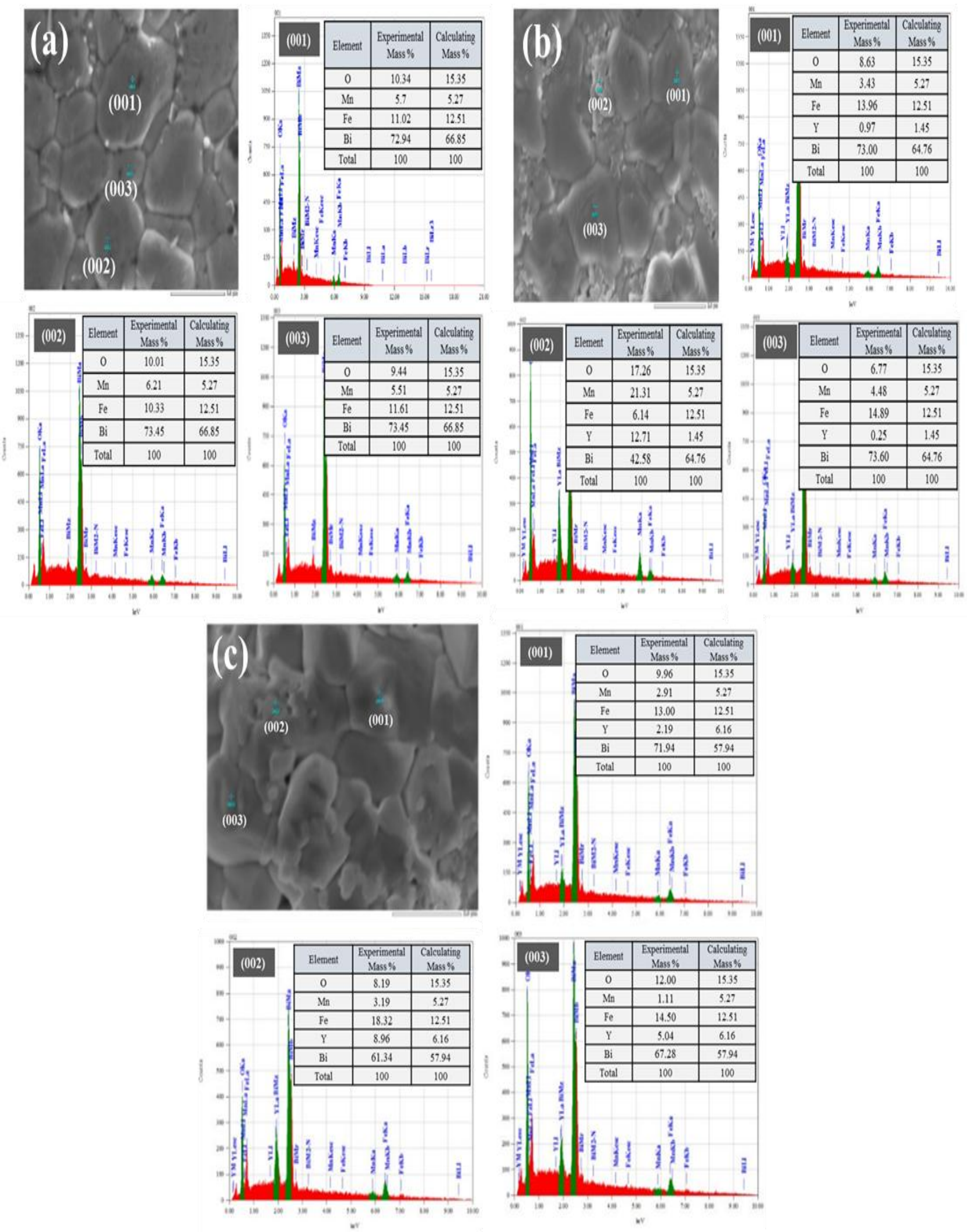

Fig. 4 EDX spectrum for $Bi_{1-x}Y_xFe_{0.7}Mn_{0.3}O_3$ samples sintered at 825°C with (a) x = 0.01 (b) x = 0.05 (a) x = 0.2.

Dielectric Properties at Room Temperature

In Fig. 5 (a), the graph shows how ε′ changes with frequency. From the graph, it appears that the dielectric constant initially decreases with increasing frequency up to 10 kHz for both undoped and doped samples, then becomes nearly constant up to 1 MHz. This behavior can be explained by the polarization model of Maxwell (Fiebig et al., 2002) and Wagner (Maxwell, 1973), consistent with Koop's phenomenon theory (Koops, 1951). Now the effect of yttrium doping on the dielectric properties of $Bi_{1-x}Y_xFe_{0.7}Mn_{0.3}O_3$ ceramics can be interpreted based on oxygen vacancies and Fe^{3+} ions (Pattanayak et al., 2014; Jonscher, 1977). Fig. 5(a) demonstrates that there is a direct correlation between the Y content and an increase in ε′. This increase arises from the isovalent substitution of volatile Bi^{3+} ions by non-volatile Y^{3+} ions.

(a)

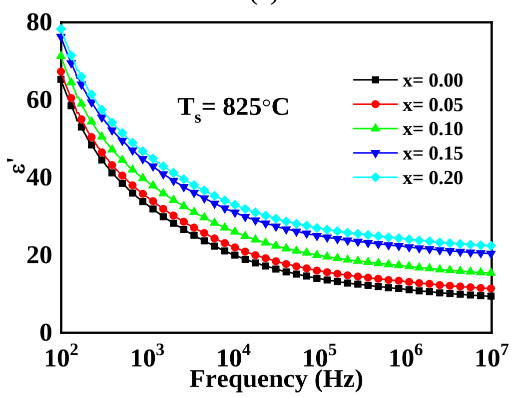

(b)

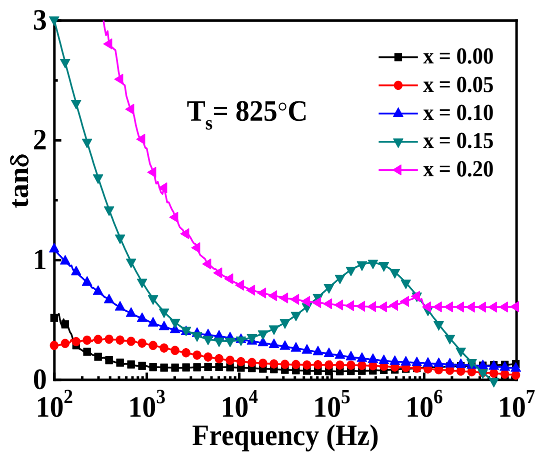

Fig. 5 Variation of (a) dielectric constant ε′ and (b) dielectric loss with frequency for various $Bi_{1-x}Y_xFe_{0.7}Mn_{0.3}O_3$ sintered at 825 °C.

That kind of substitution attenuates the formation of oxygen vacancies. The presence of Y^{3+} ions is believed to stabilize the valence states of Fe^{3+} and Fe^{2+}, thereby mitigation of oxygen vacancy concentration. This reduction in oxygen vacancies directly correlates with the observed improvement in dielectric properties, as shown in Fig. 5(a). Fig. 5(b) illustrates how the dielectric loss (tan δ) changes as a function of frequency. Its value is high at low frequencies, then its value decreases as the frequency increases. However, there is an upward trend at high frequencies for the x = 0.15 sample, which may be attributed to polarization relaxation (Barick et al., 2011).

AC conductivity

Conductivity is a fundamental property of a material, as it provides insight into the material's electrical behaviour. Understanding the conduction mechanisms in multiferroic compounds like BYFMO is crucial, as their conductivity is governed by a combination of electronic and ionic (Mukherjee, 2014). Fig. 6(a) illustrates the frequency-dependent AC conductivity (σ_{ac}) of $Bi_{1-x}Y_xFe_{0.7}Mn_{0.3}O_3$ multiferroic ceramics with two distinct conductive regions at room temperature. One region stays at a low frequency. In which σac remains relatively constant and reflects the intrinsic DC conductivity (σ_{dc}). And another region stays at a high frequency. In that case, σac rapidly increases, indicates enhanced charge-carrier hopping between localized sites. This hopping phenomenon can be explained by an increase in the conductive grain at higher frequencies (Macdonald, 1992). There is Jonscher's power law (Jonscher, 1977), shown in the following equation below. It can explain the frequency dependence of σ_{ac}.

$$\sigma_{ac}(\omega) = \sigma_{dc} + B\omega^n$$

where the exponent 'n' quantifies the interaction between mobile ions and the surrounding lattice, with values ranging from 0 to 1. The observed increase in conductivity with frequency, as shown in Fig. 6(b), suggests a small polaron hopping mechanism in the conduction process. Further, it is supported by the frequency exponent 'n' values, determined from the slope of log(σac) vs. logω curves shown in Fig. 6(b), which stay less than unity ($0.433 \leq n \leq 0.916$). This trend is consistent with previous reports on doped BFO (Das et al., 2012; Khandekar et al., 2011).

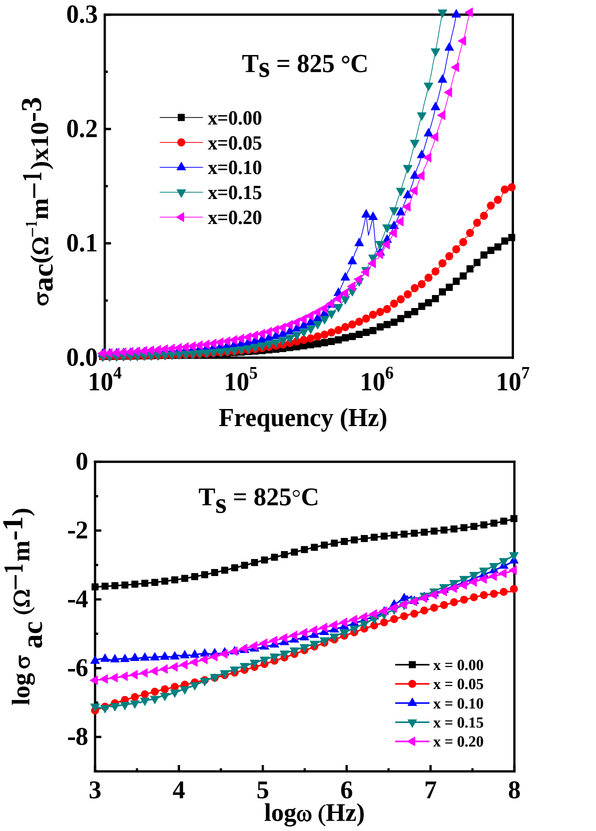

Fig. 6(a) Variation of ac conductivity with frequency and (b) *logσ* as *logω* for various Bi$_{1-x}$YxFe$_{0.7}$Mn$_{0.3}$O$_3$ sintered at 825 ºC.

Additionally, it is observed that σ_{ac} increases with increasing Y content. This improvement is ascribed to an increased number of charge carriers.

Complex Impedance Spectra Analysis

Fig. 7(a) displays the change in the real part of impedance ($Z^/$) with frequency at room temperature for different $Bi_{1-x}Y_xFe_{0.7}Mn_{0.3}O_3$ samples sintered at 825°C with x values of 0.00, 0.05, 0.10, 0.15, and 0.20. As shown in this figure, the $Z^/$ value gradually decreases as the frequency increases up to a certain limit, 10 kHz, after which its frequency dependence becomes negligible. At higher frequencies, a constant $Z^/$ ensures higher conductivity. At lower frequencies, the observation of higher impedance ($Z^/$) values indicates that the materials exhibit greater polarization effects. This effect is likely due to the presence of all types of polarization mechanisms, including dipolar, interfacial, and electronic polarization, at lower frequencies. All compositions exhibited similar impedance values ($Z^/$) at higher frequencies. This convergence indicates the potential for space charge polarization to be released (Behera et al., 2008). Moreover, the undoped sample displayed lower impedance compared to its doped counterparts. Fig. 7(b) illustrates how the imaginary part of the complex impedance ($Z^{//}$) changes with frequency for $Bi_{1-x}Y_xFe_{0.7}Mn_{0.3}O_3$ compositions sintered at 825°C for 2 hours each. The behavior observed in Fig. 7(b) with respect to frequency is similar to that of $Z^/$.

(a)

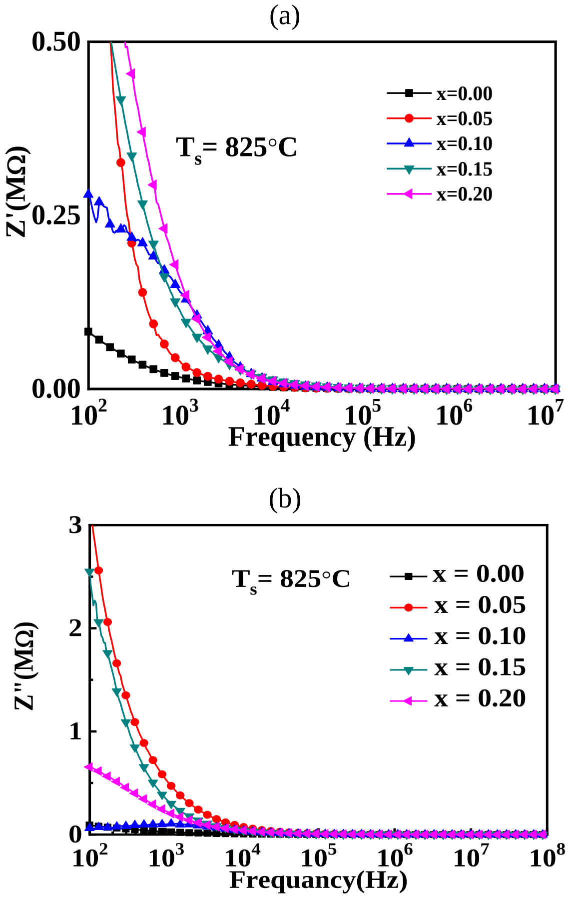

Fig. 7(a) Variation of (a) Z′ and (b) Z″ with the frequency for $Bi_{1-x}Y_xFe_{0.7}Mn_{0.3}O_3$ samples.

Table 1. Grain and grain boundary resistance of various $Bi_{1-x}Y_xFe_{0.7}Mn_{0.3}O_3$ compositions.

Composition, x	0.00	0.05	0.10	0.15	0.20
R_g (MΩ)	0.28	41.28	99.99	190.7	199.02
R_{gb} (MΩ)	37.00				

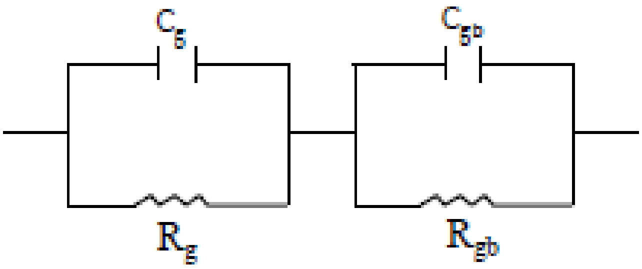

Fig. 8(a) Electrical equivalent circuit of CIS.

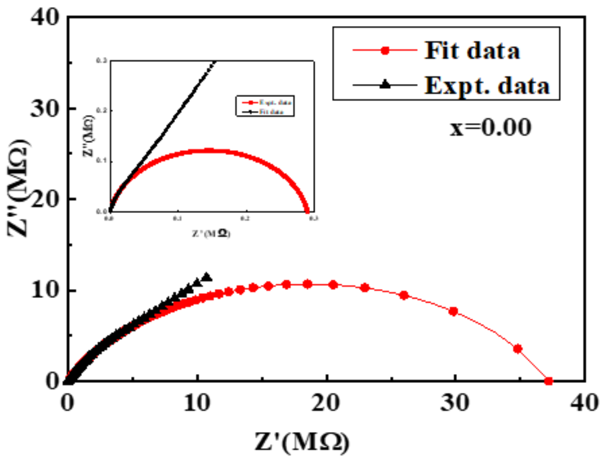

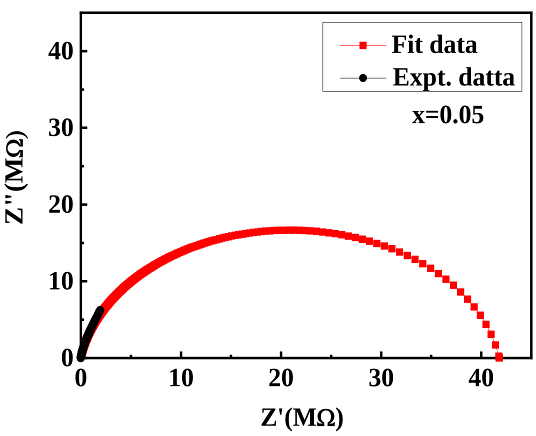

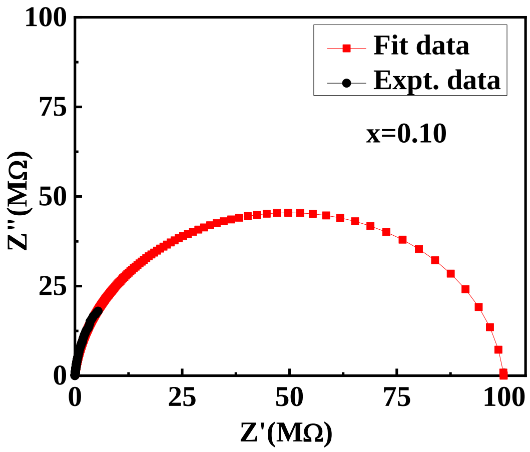

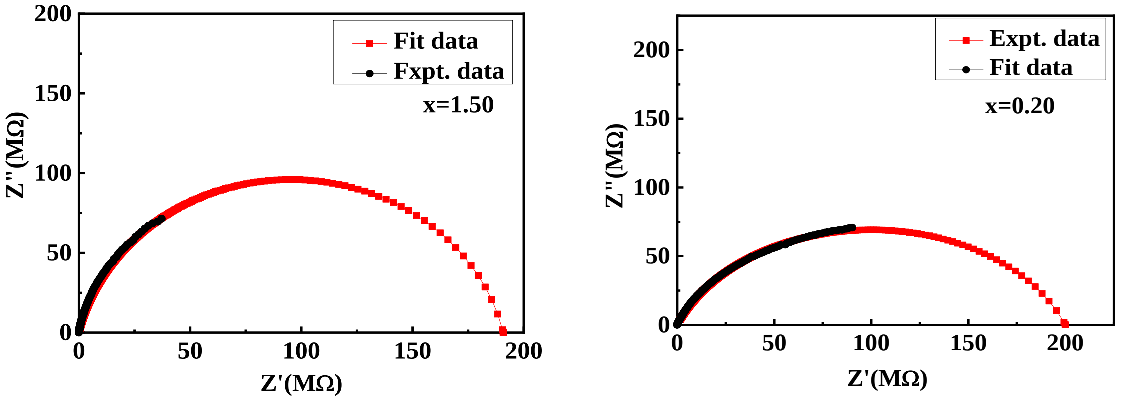

Fig. 8(b) Cole–Cole plots of Z/ and Z// at room temperature for various $Bi_{1-x}Y_xFe_{0.7}Mn_{0.3}O_3$ samples.

Cole-Cole Plot Analysis

Here, impedance is measured for all samples. Impedance spectroscopy is used to measure impedance. It analyzes all contributions to impedance for the bulk grain, grain boundary, and electrode interface of a material. These contributions characterized by plotting successive semicircles in the complex plane, known as Cole-Cole plots, in the complex plane. This plot is the imaginary part plotted against the real part (Macdonald et al., 2018; Zhu et al., 2001). An ideal Cole-Cole plot consists of perfect semicircles, and its centers sit on the real axis. But when a pot is drawn using experimental data, it often deviates from the ideal plot due to various factors (Kumar et al., 2000). In the plot, a high-frequency semicircle is attributed to grain/bulk resistance, a low-frequency semicircle to ion and electron transfers at the electrode-sample interface, and an intermediate-frequency semicircle to grain boundary resistance (Pattanayak et al., 2014). These contributions can vary with temperature, and not all may be observed within a given frequency range. To analyze the impedance data, an equivalent circuit consisting of two parallel RC circuits connected in series was employed in Fig. 8(a). In the present study, the impedance spectrum, which features two overlapping semicircular arcs, was modeled using an equivalent circuit. This circuit consists of two parallel resistor-capacitor (RC) elements: one representing the grain (Rg and Cg), and the other representing the grain boundary (Rgb and Cgb).

Each RC element represents a grain and a grain boundary and corresponds to a semicircle in the Cole-Cole plot. Fig. 8(b) shows the Cole-Cole plots for different $Bi_{1-x}Y_xFe_{0.7}Mn_{0.3}O_3$ compositions measured at room temperature. The distorted semicircular arcs are observed in both high- and low-frequency regions and indicate non-Debye-type relaxation (West et al., 1997) for all the samples. By fitting the simulated data to depressed/distorted semicircles as shown in Fig. 8(b), it was found that the sample with x = 0.00 exhibited two semicircles, samples with 0.05 < x < 2.00 showed only one semicircle, and all semicircles originated from the origin of the axis. This suggests that, at room temperature, the dominant conductivity mechanism in the majority of samples is primarily grain-boundary-related. When a Cole-Cole plot shows only a single semicircle after doping, it typically means the grain boundary resistance has become negligible compared to the grain resistance, so the two responses are no longer distinct. The increasing arc diameter with higher Y content indicates an increase in grain resistance (R_g). The higher R_g values with increasing Y content can be explained by the observed microstructural changes and the decrease in oxygen vacancy defects. The values of R_g and grain boundary resistance (R_{gb}) were calculated from the intercepts on the Z' axis and are listed in Table 1.

Conclusions

In this study, $Bi_{1-x}Y_xFe_{0.7}Mn_{0.3}O_3$ ceramics were successfully synthesized using the conventional solid-state reaction method. All samples were sintered at 800°C, 825°C, and 850°C. Investigation of the influence of sintering temperature on the bulk density of the samples showed that bulk density increased, peaked at 825°C, and then declined. Therefore, 825°C is the optimal sintering temperature for all samples. XRD patterns confirmed a rhombohedral R3c crystal structure for all samples. And its primary peaks aligned closely with BiFeO3 (JCPDS Card No. 71-2494). Secondary phases such as $Bi_2Fe_4O_9$ and $Bi_{25}FeO_{40}$ were present. The decreasing trend in tolerance factor (t) from 0.84023 to 0.83124 with increasing Y doping led to a structural distortion in the perovskite lattice. FESEM analysis confirmed that randomly oriented microstructures, unevenly sized grains, and significant intergranular porosity were present in all samples. Average grain sizes **(**D) measured by ImageJ software were found in the range of 1.22 to 1.89 μm. EDX spectroscopy analysis confirmed the presence of raw elements in the samples, although slight variations in composition ratios were visible across the surfaces. The dielectric properties of all samples ensured a decrease in ε′ with increasing frequency up to 10 kHz, after which it stabilized up to 1 MHz. The effect of Yttrium on the dielectric properties of the samples also showed that ε′ was enhanced due to a reduction in oxygen vacancies. The frequency-dependent behaviour of σ_{ac} of all samples followed Jonscher's power law. σ_{ac} enhanced with increasing Y content due to a greater number of charge carriers, provided insights into the electrical conduction mechanisms in these multiferroic ceramics. Impedance analysis of all samples made sure that a frequency-dependent decrease in the real part of impedance (Z') up to 10 kHz, which indicates enhanced conductivity at higher frequencies. Impedance spectroscopy of all samples revealed non-Debye-type relaxation with conductivity dominated by grain effects in Y-doped samples. From Cole-Cole plots, a transition from two semicircles (x = 0.00) to a single semicircle (x = 0.05–0.20) was observed, indicated reduced grain boundary contributions to resistance. The increase in grain resistance (Rg) with higher Y content verified the decrease in oxygen vacancy defects and microstructural changes confirmed by equivalent circuit modelling. Finally, increased AC conductivity and optimized dielectric properties make $Bi_{1-x}Y_xFe_{0.7}Mn_{0.3}O_3$ ceramics promising for multiferroic devices, including capacitors, spintronic devices, and high-frequency applications.

Acknowledgment

The authors thank the Committee for Advanced Studies & Research (CASR) at BUET for their financial support. They also express their gratitude to the Microstructural Analysis Unit at the University of Technology Sydney, Australia, for granting access to the X-ray diffractometer facility.

Authors contribution

Sonet Kumar Saha conducted all experimental investigations and prepare samples, acquired data, and performed subsequent analysis. He also drafted the conceptual framework and the initial manuscript version. Md. Ashraf Ali performed a critical review of the manuscript and provided editorial contributions. A. K. M. Akther Hossain provided overall project supervision and intellectual guidance.

Conflict of interest

The authors declare that they have no competing interests.

References

Agrawal AK, Kumari A, Kumar B, Kumar P, Jena LK, Asthana S, Singh RK and Jaiswal SK. Structural, optical absorption and electrical characteristics of sol-gel synthesized chromium-doped bismuth ferrites. *Phys. B: Condens. Matter* 2025; 696: 416639.

Barick BK, Mishra KK, Arora AK, Choudhary RNP and Pradhan DK. Impedance and Raman spectroscopic studies of $(Na_{0.5}Bi_{0.5})TiO_3$. *J. Phys. D: Appl. Phys.* 2011; 44(35): 355402.

Basiri MH, Shokrollahi H and Isapour G. Effects of La content on the magnetic, electric and structural properties of $BiFeO_3$. *J. Magn. Magn. Mater.* 2014; 354: 184-189.

Behera B, Nayak P and Choudhary RNP. Structural and electrical properties of $KCa_2Nb_5O_{15}$ ceramics. *Cent. Eur. J. Phys.* 2008; 6: 289-295.

Chauhan S, Arora M, Sati PC, Chhoker S, Katyal SC and Kumar M. Structural, vibrational, optical, magnetic and dielectric properties of $Bi_{1-x}Ba_xFeO_3$ nanoparticles. *Ceram. Int.* 2013; 39(6): 6399-6405.

Chen CC. Study on the ferroelectric and magnetic properties of $BiFe_{1-x}Mn_xO_3$ polycrystalline ceramics dependence on the Mn content. *J. Ceramic Process. Res.* 2014; 15(6): 424-427.

Chen J, Dai H, Li T, Liu D, Xue R, Xiang H and Chen Z. Role of Mn substitution in the multiferroic properties of $BiFeO_3$ ceramics. *J. Supercond. Novel Magn.* 2015; 28: 2751-2754.

Chen SY, Wang L, Xuan H, Zheng Y, Wang D, Wu J, Du Y and Huang Z. Multiferroic properties and converse magnetoelectric effect in $Bi_{1-x}Ca_xFeO_3$ ceramics. *J. Alloys Compd.* 2010; 506(2): 537-540.

Chung CF, Lin JP and Wu JM. Influence of Mn and Nb dopants on electric properties of chemical-solution-deposited $BiFeO_3$ films. *Appl. Phys. Lett.* 2006; 88: 242909.

Dao VT, Du Thi XT and Nguyen VM. Structural and physical properties of Y-doped $BiFeO_3$ material prepared by sol-gel method. *VNU J. Sci. Math.-Phys.* 2013; 29(3): 63-69.

Das Adhikary G, Muleta GJ, Tina GA, Sharma D, Mahale B, Silva LL, Hinterstein M, Senyshyn A and Ranjan R. Structural insights into electric field induced polarization and strain responses in $K_{0.5}Na_{0.5}NbO_3$ modified morphotropic phase boundary compositions of $Na_{0.5}Bi_{0.5}TiO_3$-based lead-free piezoelectrics. *Phys. Rev. B,* 2023; 107(13): 134108.

Das R, Sarkar T and Mandal K. Multiferroic properties of Ba^{2+} and Gd^{3+} co-doped bismuth ferrite: magnetic, ferroelectric and impedance spectroscopic analysis. *J. Phys. D: Appl. Phys.* 2012; 45(45): 455002.

Fiebig M, Lottermoser T, Fröhlich D, Goltsev AV and Pisarev RV. Observation of coupled magnetic and electric domains. *Nature* 2002; 419(6909): 818-820.

Gautam A, Uniyal P, Yadav KL and Rangra VS. Dielectric and magnetic properties of $Bi_{1-x}Y_xFeO_3$ ceramics. *J. Phys. Chem. Solids* 2012; 73(2): 188-192.

Gu Y, Zhao J, Zhang W, Liu S, Ge S, Chen W and Zhang Y. Improved ferromagnetism and ferroelectricity of La and Co co-doped $BiFeO_3$ ceramics with Fe vacancies. *Ceram. Int.* 2016; 42(7): 8863-8868.

Huong TN, Luu Thu HA, Nguyen Long N and Nguyen Hong H. Crystal structure and magnetic properties for $Bi_{1-x}Eu_xFeO_3$ compounds. *VNU J. Sci. Math.-Phys.* 2017; 33(1): 35-40.

Jonscher AK. The universal dielectric response. *Nature* 1977; 267(5613): 673-679.

Karimi S, Reaney IM, Levin I and Sterianou I. Nd-doped $BiFeO_3$ ceramics with antipolar order. *Appl. Phys. Lett.* 2009; 94(11): 112903.

Khandekar MS, Kambale RC, Patil JY, Kolekar YD and Suryavanshi SS. Effect of calcination temperature on the structural and electrical properties of cobalt ferrite synthesized by combustion method. *J. Alloys Compd.* 2011; 509(5): 1861-1865.

Koops CG. On the dispersion of resistivity and dielectric constant of some semiconductors at audio frequencies. *Phys. Rev.* 1951; 83(1): 121.

Kumar MM, Srinivas A and Suryanarayana SV. Structure property relations in $BiFeO_3/BaTiO_3$ solid solutions. *J. Appl. Phys.* 2000; 87(2): 855-862.

Luo L, Wei W, Yuan X, Shen K, Xu M and Xu Q. Multiferroic properties of Y-doped $BiFeO_3$. *J. Alloys Compd.* 2012; 540: 36-38.

Macdonald JR, Johnson WB, Raistrick ID, Franceschetti DR, Wagner N, McKubre MCH, Macdonald DD, Sayers B, Bonanos N, Steele BCH and Butler EP. *Impedance spectroscopy:*

theory, experiment, and applications. Hoboken, NJ: John Wiley & Sons; 2018. p. 424-458.

Macdonald JR. Impedance spectroscopy. *Ann. Biomed. Eng.* 1992; 20: 289-305.

Maxwell JC. *Electricity and Magnetism, Vol. 2*. New York: Oxford University Press; 1973. p. 828.

Miah MJ, Khan MNI and Hossain AKMA. Synthesis and enhancement of multiferroic properties of (x) $Ba_{0.95}Sr_{0.05}TiO_3$–(1−x) $BiFe_{0.90}Dy_{0.10}O_3$ ceramics. *J. Magn. Magn. Mat.* 2016; 397: 39-50.

Minh NNN, Hue VT, Thu NT, Hien VT, Dung DD and Quan ND. Augmentation of optical and magnetic characteristics at ambient temperature in bismuth ferrite-titanium ($BiFe_{1-x}Ti_xO_3$) multiferroic compounds. *Mater. Res. Express* 2024; 11(4): 045702.

Mukherjee A, Banerjee M, Basu S, Thanh NTK, Green LAW and Pal M. Enhanced magnetic and electrical properties of Y and Mn co-doped BiFeO3 nanoparticles. *Phys. B: Condens. Matter,* 2014; 448:199-203.

Muneeswaran M, Gopiraman M, Dhanabalan SS, Giridharan NV and Akbari-Fakhrabadi A. Multiferroic properties of rare earth-doped $BiFeO_3$ and their spintronic applications. In: *Metal and Metal Oxides for Energy and Electronics*, springer, 2021: pp. 375-395.

Palkar VR, John J and Pinto R. Observation of saturated polarization and dielectric anomaly in magnetoelectric $BiFeO_3$ thin films. *Appl. Phys. Lett.* 2002; 80(9): 1628-1630.

Pattanayak S, Choudhary RNP, Das PR and Shannigrahi SR. Effect of Dy-substitution on structural, electrical and magnetic properties of multiferroic $BiFeO_3$ ceramics. *Ceram. Int.* 2014; 40(6): 7983-7991.

Ramesh R and Spaldin NA. Multiferroics: progress and prospects in thin films. *Nat. Mater.* 2007; 6(1): 21-29.

Scott JF. Applications of modern ferroelectrics. *Science* 2007; 315(5814): 954-959.

Singh AK, Mani AD and Soibam I. Low temperature synthesis and structural, dielectric and optical studies of $Bi_{1-x}Gd_xFeO_3$ (x=0–0.15) nanoceramics. *Integr. Ferroelectrics* 2018; 193(1): 134-141.

Singh H and Yadav KL. Effect of Nb substitution on the structural, dielectric and magnetic properties of multiferroic $BiFe_{1-x}Nb_xO_3$ ceramics. *Mater. Chem. Phys.* 2012; 132(1): 17-21.

Teague JR, Gerson R and James WJ. Dielectric hysteresis in single crystal $BiFeO_3$. *Solid State Commun.* 1970; 8(13): 1073-1074.

Varshney D and Kumar A. Structural, Raman and dielectric behavior in $Bi_{1-x}Sr_xFeO_3$ multiferroic. *J. Mol. Struct.* 2013; 1038: 242-249.

Verma KC. Synthesis and characterization of multiferroic $BiFeO_3$ for data storage. In: *Bismuth-Fundamentals and Optoelectronic Applications*. *Intech Open*, 2020: 94049.

Wang N, Luo X, Han L, Zhang Z, Zhang R, Olin H and Yang Y. Structure, performance, and application of $BiFeO_3$ nanomaterials. *Nano-Micro Lett.* 2020; 12 (1): 81.

Wang YP, Zhou L, Zhang MF, Chen XY, Liu JM and Liu ZG. Room-temperature saturated ferroelectric polarization in $BiFeO_3$ ceramics synthesized by rapid liquid phase sintering. *Appl. Phys. Lett.* 2004; 84(10): 1731-1733.

West AR, Sinclair DC and Hirose N. Characterization of electrical materials, especially ferroelectrics, by impedance spectroscopy. *J. Electroceram.* 1997; 1(1): 65-71.

Wu M, Wang W, Jiao X, Wei G, He L, Han S, Liu Y and Chen D. Structural and multiferroic properties of Pr and Ti co-doped $BiFeO_3$ ceramics. *Ceram. Int.* 2016; 42(13): 14675-14678.

Wu YJ, Chen XK, Zhang J and Chen XJ. Structural transition and enhanced magnetization in $Bi_{1-x}Y_xFeO_3$. *J. Magn. Magn. Mat.* 2012; 324(7): 1348-1352.

Xu JM, Wang GM, Wang HX, Ding DF and He Y. Synthesis and weak ferromagnetism of Dy-doped $BiFeO_3$ powders. *Mater. Lett.* 2009; 63(11): 855-857.

Yin L and Mi W. Progress in $BiFeO_3$- based heterostructures: materials, properties and applications. *Nanoscale* 2020; 12(2): 477-523.

Yu B, Li M, Wang J, Pei L, Guo D and Zhao X. Enhanced electrical properties in multiferroic $BiFeO_3$ ceramics co-doped by La^{3+} and V^{5+}. *J. Phys. D: Appl. Phys.* 2008; 41(18): 185401.

Zatsiupa AA, Bashkirov LA, Troyanchuk IO, Petrov GS, Galyas AI, Lobanovsky LS and Truhanov SV. Magnetization, magnetic susceptibility, effective magnetic moment of Fe^{3+} ions in $Bi_{25}FeO_{39}$ ferrite. *J. Solid State Chem.* 2014; 212: 147-150.

Zhang ST, Zhang Y, Lu MH, Du CL, Chen YF, Liu ZG, Zhu YY, Ming NB and Pan XQ. Substitution-induced phase transition and enhanced multiferroic properties of $Bi_{1-x}La_xFeO_3$ ceramics. *Appl. Phys. Lett.* 2006; 88(16): 162901.

Zhu M, Xie H, Guo J, Bai W and Xu Z. Impedance spectroscopy analysis on electrical properties of serpentine at high pressure and high temperature. *Sci. China Ser. D: Earth Sci.* 2001; 44: 336-345.